

Cite this: *CrystEngComm*, 2014, **16**, 6066–6079

Fluorinated mixed valence Fe(II)–Fe(III) phosphites with channels templated by linear tetramine chains. Structural and magnetic implications of partial replacement of Fe(II) by Co(II)†

Joseba Orive,^a Roberto Fernández de Luis,^a Jesús Rodríguez Fernández,^b Estibaliz Legarra,^c Fernando Plazaola^c and María I. Arriortua^{*a}

Three new fluorinated mixed valence Fe(II)–Fe(III) phosphites were synthesized by employing mild hydrothermal conditions. $(H_4baepn)_{0.5}[Fe^{III}_{2.3}Fe^{II}_{1.7}(H_2O)_2(HPO_3)_{4-(x+y)}(HPO_4)_x(PO_4)_yF_4]$ ($x \approx 0.13$, $y \approx 0.3$) (**1**) ($baepn = N,N'$ -bis(2-aminoethyl)-1,3-propanediamine ($C_7N_4H_{20}$)) and the Co(II)-substituted phase with the formula $(H_4baepn)_{0.5}[Fe^{III}_{2.0}Fe^{II}_{0.71}Co^{II}_{1.29}(H_2O)_2(HPO_3)_{4-x}(HPO_4)_xF_4]$ ($x \approx 0.38$) (**2**) were studied by single crystal X-ray diffraction. The phase with the major content of Co(II), $(H_4baepn)_{0.5}[Fe^{III}_{2.0}Fe^{II}_{0.62}Co^{II}_{1.38}(H_2O)_2(HPO_3)_{4-x}(HPO_4)_xF_4]$ ($x \approx 0.38$) (**3**) was obtained as a polycrystalline powder and studied by Rietveld refinement by using the structural model of **2**. These compounds were characterized by ICP-Q-MS, thermogravimetric and thermodiffractometric analyses, and XPS, IR, UV/vis and Mössbauer spectroscopy. The single crystal data indicate that phases **1** and **2** crystallize in the $P2_1/c$ space group with lattice parameters $a = 13.6808(4)$, $b = 12.6340(2)$, $c = 12.7830(3)$ Å and $\beta = 116.983(4)^\circ$ for **1** and $a = 13.6823(4)$, $b = 12.6063(3)$, $c = 12.7535(4)$ Å and $\beta = 116.988(4)^\circ$ for **2**, with $Z = 4$. The reciprocal space of **1** shows satellite reflections with a modulation wavevector $q = 0.284(2)a^*$ which indicate an incommensurate long-range order. The average structure of these compounds is built up by a 3D lattice constructed by inorganic layers of Fe(III) chains and Fe(II) and Co(II) dimers joined by phosphite groups partially substituted by HPO_4 and PO_4 tetrahedral groups. These anionic layers stack along the [100] direction encapsulating linear tetramines in eight-membered open channels involving host–guest interactions. Magnetic measurements of **1** and **3** showed antiferromagnetic coupling as the major interactions, exhibiting a weak ferromagnetic component together with a spin glass transition at low temperature in the case of **1**. Heat capacity measurements showed a small anomaly at 20.5 K for **1** and a sharp magnetic peak at 28 K for **3**. Unexpectedly, the small anomaly observed in **1** increased with the magnetic field and became better defined.

Received 4th February 2014,
Accepted 7th May 2014

DOI: 10.1039/c4ce00264d

www.rsc.org/crystengcomm

^a Departamento de Mineralogía y Petrología, Facultad de Ciencia y Tecnología, Universidad del País Vasco (UPV/EHU), Apdo. 644, 48080 Bilbao, Spain.
E-mail: joseba.orive@ehu.es, roberto.fernandez@ehu.es, maribel.arriortua@ehu.es;
Fax: +34 946 013 500; Tel: +34 946 015 984

^b CITIMAC, Facultad de Ciencias, Universidad de Cantabria, 39005 Santander, Spain. E-mail: rodriguf@unican.es; Fax: +34 942 201 402; Tel: +34 942 201 511

^c Departamento de Electricidad y Electrónica, Facultad de Ciencia y Tecnología, Universidad del País Vasco (UPV/EHU), Apdo. 644, 48080 Bilbao, Spain.
E-mail: estibaliz.legarra@ehu.es, fernando.plazaola@ehu.es;
Fax: +34 946 013 500; Tel: +34 946 015 940

† Electronic supplementary information (ESI) available: View of the reciprocal space and reconstruction of the $h0l$ layers of **1** and **2**, conformers A and B of the organic molecule, Rietveld structure analysis of **3**, thermal ellipsoid plots of **1** and **2**, thermal analysis, infrared spectra, XPS spectra, magnetization vs. applied magnetic field at different temperatures for **3**, thermoremanent magnetization and ac magnetic susceptibility of **1**, magnetic pathways and thermal evolution of C_p , C_{phon} , and C_{mag} of phases **1** and **3**. CCDC 978254 and 978255. See DOI: 10.1039/c4ce00264d

Introduction

One of the challenges faced in the field of open framework materials science and technology is the design and synthesis of porous compounds which combine the classical properties of the zeolites with physicochemical properties such as magnetic, optical or conductive arising from the introduction of transition metals in the crystalline structures.^{1,2}

Synthesis of microporous materials such as zeolites, aluminosilicates and phosphates or other zeotypes, which has attracted interest because of their potential industrial applications as solid acid catalysts, ion exchangers or in the separation of gases,^{2,3} is driven sometimes by using protonated amines as templates or structure directing agents (SDAs).⁴

By employing small organic amines as structure-directing agents, such as *n*-propylamine, *n*-butylamine, cyclopentylamine

and cyclohexylamine, extra-large-micropore compounds, for instance 16 and 18-membered-ring fluorinated gallium phosphates,⁵ vanadium(IV) phosphites with 16-ring channels⁶ and zinc phosphites with 24-ring channels,⁷ have been hydrothermally obtained. Their crystallization is given by a cooperative templating mechanism of multiple organic cations which reside within the voids with their hydrophobic groups pointing toward the center of the pores and the hydrophilic NH_3^+ ends interacting *via* hydrogen bonding with the host.

The assembly of small organic amines and their effect as SDAs on the crystallization of large micropore aluminophosphites, zincophosphates, and aluminophosphates have also been investigated. The authors conclude that the aggregation of 1,6-hexanediamine (HDA) molecules gives rise to the formation of lamellar structures, while microporous 3D frameworks are formed mainly from the host–guest interaction between inorganic frameworks and individual 1,6-HDA molecules.⁸

Recently, a series of gallium zincophosphites, NTHU-13, the channel ring size of which can be expanded from 24-ring to 72-ring, were successfully achieved by using heterometal centers and a series of aliphatic monoamines; the template size was increased from 4-carbon (4C) containing butylamine to 18C octadecylamine.⁹

According to the host–guest charge matching concept a highly charged inorganic framework should be templated by highly charged organic amines such as multiamines.¹⁰ For instance, the chain-type polyamines such as TETA (10-atom-skeleton tetramine),¹¹ AE-DAP (8-atom-skeleton triamine)¹² and 1,6-HDA (8-atom-skeleton diamine)¹³ were used in the crystallization of $(\text{C}_6\text{H}_{22}\text{N}_4)_{0.5}[\text{Zn}_3(\text{HPO}_4)_2(\text{PO}_4)_2]$ (16R-channel structure with 25.6% non framework space (NFS)), $(\text{C}_5\text{H}_{18}\text{N}_3)_{0.5}[\text{Zn}_3(\text{HPO}_4)_3(\text{PO}_4)]$ (16R-channel structure with 36.2% NFS) and $(\text{C}_6\text{H}_{18}\text{N}_2)[\text{Zn}_4(\text{PO}_4)_2(\text{HPO}_4)_2] \cdot 3\text{H}_2\text{O}$ (20R-channel structure with 45.7% NFS), respectively. The role of such templates indicates that the size effect of a polyamine template is reduced with increasing number of amino groups and that NFS in the structures increases in proportion to the channel size. However, W.-M. Chang *et al.* observed opposite template effects in the synthesis of zinc phosphates with 16R channel structures by using linear triamine and pentamine molecules. They concluded that the NFS is substantially augmented with increasing length and amino groups in the template.¹⁴

Even today the specific templating role of the SDAs is not clear. In fact, the ‘true’ templating effect referring to a direct correlation between the van der Waals shape of the organic template and the channel space of the resultant inorganic framework is not very usual.¹⁵ In that regard, computer modeling has demonstrated to be a useful tool for examining nonbonding interaction energies of different host–guest systems.¹⁶

In spite of the scientific community having made progress in the rational organic SDA-mediated synthesis of zeolitic inorganic open framework materials,⁴ the complex chemical reaction mechanisms in which the inorganic buildings nucleate around the organic cationic species are still poorly understood.

Actually, there are many examples in which the SDAs represent the products of the initial organic precursors transformed during the hydrothermal synthesis by means of hydrolysis of linear polyamines,¹⁷ decomposition of amides¹⁸ or *N*-alkylation reactions.¹⁹ Therefore, because the large number of parameters involved in the reaction processes still make the rational approach to the synthesis of these materials a challenging task, the “trial-and-error” strategy becomes necessary to explore new architectures when new organic templates are being used.

On the other hand, the total or partial replacement of the classical four-coordinated PO_4^{3-} building units by 3-connected groups such as the pseudo-pyramidal HPO_3^{2-} blocks gives rise to different connectivity patterns which can favor the construction of open structures with novel topologies and lower framework densities.²⁰ Moreover, the networks containing transition metal ions with open d shells are attractive due to their potential magnetic properties. More specifically, mixed-valence iron-containing compounds may exhibit interesting magnetic behaviour such as ferrimagnetism,²¹ spin glass states,^{22,23} or spin canted antiferromagnetism.²⁴ In particular, the literature refers to the existence of two examples of mixed-valence iron purely inorganic phosphites, $\text{Li}_{1.43}[\text{Fe}^{\text{II}}_{4.43}\text{Fe}^{\text{III}}_{0.57}(\text{HPO}_3)_6] \cdot 1.5\text{H}_2\text{O}$ ²³ and $\text{Fe}^{\text{II}}_{2.08}\text{Fe}^{\text{III}}_{0.42}(\text{H}_2\text{O})_2(\text{HPO}_3)_{1.58}(\text{PO}_4)_{0.42}\text{F}$,²⁵ and three examples of mixed-valence iron organically templated phosphites, $(\text{NH}_4)[\text{Fe}^{\text{II}}\text{Fe}^{\text{III}}(\text{HPO}_3)_4]$,²⁶ $(\text{C}_4\text{H}_{12}\text{N}_2)[\text{Fe}^{\text{II}}\text{Fe}^{\text{III}}(\text{HPO}_3)_2\text{F}_3]$ ²⁷ and $(\text{C}_4\text{N}_2\text{H}_{12})[\text{Fe}^{\text{II}}_{0.86}\text{Fe}^{\text{III}}_{1.14}(\text{HPO}_3)_{1.39}(\text{HPO}_4)_{0.47}(\text{PO}_4)_{0.14}\text{F}_3]$.²⁸

In addition, many times the design and synthesis of magnetic materials is based on the study of replacing the transition metals. For example, cobalt–iron bimetallic molecular magnets based on cyano-bridged coordination polymers²⁹ (Prussian Blue analogues) and oxalate-bridged complexes³⁰ have been of great interest due to their functional magnetic properties, such as photoinduced magnetism,³¹ anisotropic photoinduced magnetism in thin films,³² and a charge-transfer-induced spin transition.³³

In this work, in order to satisfy the host–guest charge matching principle,¹⁰ the choice of the chain-type tetramine *N,N'*-bis(2-aminoethyl)-1,3-propanediamine (baepn = $\text{C}_7\text{N}_4\text{H}_{20}$) as the structure directing agent, which may become highly charged, was accompanied by the introduction of F^- anions; the amine also plays the role of a template stabilizing the construction of the resulting network. While this molecule has been used for the construction of some transition metal coordination polymers,³⁴ wherein the organic ligand is coordinated by its four nitrogen atoms to the equatorial plane of the metallic polyhedra, we ignore its use in the synthesis of zeotypes or related compounds.

In this paper, we report on the hydrothermal synthesis, crystal structure determination, the spectroscopic behaviour and thermal and magnetic properties of $(\text{H}_4\text{baepn})_{0.5}[\text{Fe}^{\text{III}}_{2.3}\text{Fe}^{\text{II}}_{1.7}(\text{H}_2\text{O})_2(\text{HPO}_3)_{4-(x+y)}(\text{HPO}_4)_x(\text{PO}_4)_y\text{F}_4]$ ($x \approx 0.13, y \approx 0.3$) (1). The partial replacement of $\text{Fe}(\text{II})$ by $\text{Co}(\text{II})$ has given rise to $(\text{H}_4\text{baepn})_{0.5}[\text{Fe}^{\text{III}}_{2.0}\text{Fe}^{\text{II}}_{0.71}\text{Co}^{\text{II}}_{1.29}(\text{H}_2\text{O})_2(\text{HPO}_3)_{4-x}(\text{HPO}_4)_x\text{F}_4]$ ($x \approx 0.38$) (2) as single crystals and $(\text{H}_4\text{baepn})_{0.5}[\text{Fe}^{\text{III}}_{2.0}\text{Fe}^{\text{II}}_{0.62}\text{Co}^{\text{II}}_{1.38}(\text{H}_2\text{O})_2(\text{HPO}_3)_{4-x}(\text{HPO}_4)_x\text{F}_4]$

($x \approx 0.38$) (3), as a polycrystalline sample. The structural influence of the introduction of Co(II) ions studied by means of the analysis of the crystal structures of 1 and 2 will be discussed. Moreover, the differences in the magnetic properties between 1 and the phase with the major content of cobalt obtained, 3, will be analyzed.

Experimental section

Synthesis and characterization

Compounds 1, 2 and 3 were obtained as pure phases from different reactions. The synthetic procedure consists of dissolving a mixture of H_3PO_3 (7.5 mmol) and the metal salts ($FeCl_3$, 0.45 mmol for 1; $FeCl_3:CoCl_2$, 0.3:0.3 mmol for 2 and $FeCl_3:CoCl_2$, 0.525:0.525 mmol for 3) in 30 ml of distilled water. Then, 0.5 ml (13.9 mmol) of HF was added to the resulting solution and finally the pH was increased to approximately 2.5 by adding dropwise the organic molecule N,N -bis(2-aminoethyl)-1,3-propanediamine ($C_7N_4H_{20}$). The reaction mixtures were sealed in a PTFE-lined stainless steel pressure vessel (fill factor: 65%) and heated for 4 days at 170 °C. After the reaction, black tabular single crystals of 1 and purplish prismatic single crystals and powder of 2 and 3, respectively, were obtained. The yield of the three compounds is around 50–60% (based on the iron reagent). The existence of Co in the samples was confirmed by XRF as a preliminary characterization test.

After many attempts, compound 2 represents the phase as single crystals with the higher cobalt content achieved. That compound 3 was obtained reveals that it is possible to achieve higher cobalt contents as a powder sample. However any attempt to increase the cobalt content of the $FeCl_3:CoCl_2$ molar ratio resulted in the crystallization of the purely inorganic fluorinated Co(II) phosphite $Co_{2.5}(H_2O)_2(HPO_3)_2F^{25}$ as an impurity.

Several attempts to replace the organic template by mobile cations such as Li^+ or Na^+ were made in order to obtain a new phase with conductive properties. However, hydroxides from lithium and/or sodium sources seem to merely basify the dissolution, causing the decomposition of the organic molecule in such a way that iron(III) phosphite ($C_4N_3H_{14})[Fe_3(HPO_3)_4F_2(H_2O)_2]$ ³⁵ crystallizes.

The metal ion and phosphorous contents were confirmed by inductively coupled plasma quadrupole mass spectrometry (ICP-Q-MS) analysis, performed using a Thermo Scientific XSeries 2 spectrometer. The amount of the fluoride anion was calculated by using a selective electrode and the amounts of C, N and H were calculated by elemental analysis. $(H_4baepn)_{0.5}[Fe^{III}_{2.3}Fe^{II}_{1.7}(H_2O)_2(HPO_3)_{4-(x+y)}(HPO_4)_x(F_4)]$ ($x \approx 0.13$, $y \approx 0.3$) (1). Calculated (%): Fe, 30.02; P, 16.65; F, 10.21; C, 5.65; N, 3.77; H, 2.67. Found (%): Fe, 29.7(4); P, 16.4(3); F, 9.8(3); C 5.4(4); N, 3.5(2); H, 2.6(1). $(H_4baepn)_{0.5}[Fe^{III}_{2.0}Fe^{II}_{0.71}Co^{II}_{1.29}(H_2O)_2(HPO_3)_{4-x}(HPO_4)_x(F_4)]$ ($x \approx 0.38$) (2). Calculated (%): Fe, 20.25; Co, 10.17; P, 16.57; F, 10.17; C, 5.62; N, 3.75; H, 2.70. Found (%): Fe, 20.3(3); Co, 10.2(3); P, 16.8(3); F, 10.0(3); C 5.7(4); N, 3.6(2); H, 2.7(1).

$(H_4baepn)_{0.5}[Fe^{III}_{2.0}Fe^{II}_{0.62}Co^{II}_{1.38}(H_2O)_2(HPO_3)_{4-x}(HPO_4)_x(F_4)]$ ($x \approx 0.38$) (3). Calculated (%): Fe, 19.57; Co, 10.88; P, 16.57; F, 10.16; C, 5.62; N, 3.75; H, 2.70. Found (%): Fe, 19.6(3); Co, 10.9(3); P, 16.7(3); F, 10.3(3); C 5.5(4); N, 3.8(2); H, 2.7(1).

The densities of the three phases measured by flotation using a mixture of CH_2I_2 and $CHCl_3$ were 2.50(3) g cm⁻³ for 1, 2.51(3) g cm⁻³ for 2, and 2.51(2) g cm⁻³ for 3.

Single crystal X-ray diffraction study

High quality single crystals of 1 and 2 were selected under a polarizing microscope and mounted on a glass fiber. Intensity data were collected at 100 K using an Agilent Supernova diffractometer using a CCD (Eos) detector. Data frames were processed (unit cell determination, intensity data integration, correction for Lorentz and polarization effects,³⁶ and analytical absorption correction³⁷ taking into account the size and shape of the crystals) using the corresponding diffractometer software package.³⁸

Reciprocal space analysis of compound 1 revealed the presence of weak reflections not arbitrarily distributed but are equidistant from the main reflections along the a^* axis (Fig. S1†). These additional less intense peaks, referred to as satellite reflections, are the result of the existence of a structural modulation periodic in nature, which describes long-range order. The modulation wavevector which describes the first-order satellites with respect to the main reflections is $q = 0.284(2)a^*$ (Fig. 1), allowing the indexing of the diffraction pattern to four indices $hklm$. However, the low intensity of the satellite reflections together with the existence of diffuse scattering (Fig. S2†) hinder the superspace group and the atomic modulation functions were determined in order to describe the incommensurately modulated superstructure. While satellite reflections mark an incommensurate long-range order, the diffuse scattering processes suggest the existence of a certain disorder, dynamic or static, that breaks slightly the crystallographic order. On the other hand, compound 2 shows neither satellites nor diffuse scattering (Fig. 1 and S2†).

Therefore, we focused on the average structures, ignoring the satellite reflections. The structures were solved by direct methods, using the SHELXS 97 computer program,³⁹ in the monoclinic space group $P2_1/c$ and then refined by the full matrix least-squares procedure based on F^2 using the SHELXL 97 computer program⁴⁰ included in the WINGX software package.⁴¹ This procedure allowed us to find the positions of the iron and phosphorous atoms, and all the other non-hydrogen atoms (F, O, C and N) were placed from subsequent Fourier-difference map calculations.

For both compounds, half an organic molecule is located in the asymmetric unit and a symmetry centre generates the other half causing a symmetry disorder of the C(4) atom with an occupation factor of 0.5, giving rise to the existence of two conformers (A and B). Due to this peculiarity, a hydrogen disorder system was modeled for the parent C(3) atom, which is bonded to C(4) (Fig. S3†). Isotropic thermal displacements were used for carbon and nitrogen atoms.

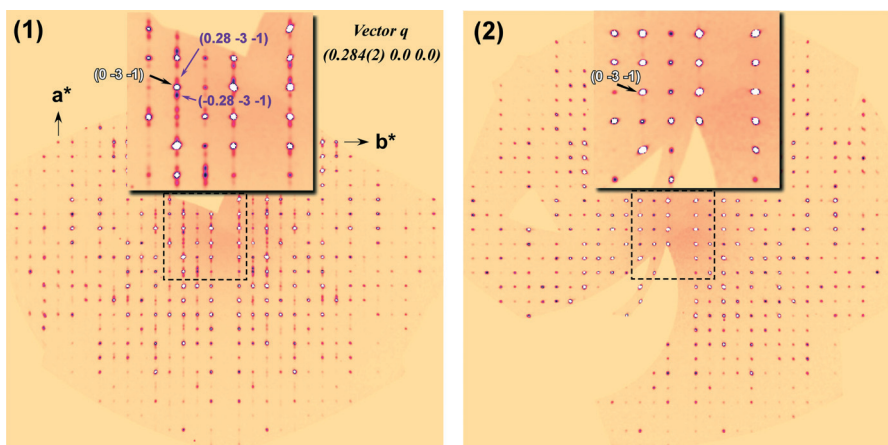


Fig. 1 Experimental images of the hk-1 layers of the diffraction patterns of **1** and **2** reconstructed using the CrysAlisPro software package.³⁸

From subsequent Fourier-difference map calculations, electron-densities exceeding $1.0 \text{ e}^{-} \text{\AA}^{-3}$ and very long $P\text{-}Q$ distances for apical hydrogen were observed near P(1), P(2) and P(3). The presence of both phosphite and phosphate groups was considered in these phosphorus sites. The existence of hydrogen phosphate groups, $(\text{HPO}_4)^{2-}$, was deduced from electroneutrality requirements. Hydrogen and oxygen atoms involved in the anionic phosphorous group replacements were treated as disordered ones with complementary occupation factors. In order to model correctly the disorder systems, the P-H (1.30(1) Å) and P-O (1.50(1) Å) bonds were restrained to the ideal values. Moreover, in order to maintain the geometry of the $(\text{HPO}_3)^{2-}$ groups, the three distances of the apical hydrogen atoms to their corresponding oxygen atoms forming the pseudotetrahedra base were refined as a variable.

For compound **2**, Co^{2+} ions should be located in the M(3) and M(4) sites given the metal-ligand distances. The best fit provides a full occupation of the M(4) position and an occupation factor of 0.3(1) for M(3) in good agreement with the chemical analysis.

For the final refinement of compounds **1** and **2**, the hydrogen atoms related to the coordinated water molecules were first located and placed in geometrically ideal positions (O-H: 0.82(1) Å; H-H: 1.35(2) Å) and refined using the riding model. Anisotropic thermal parameters were used for all the atoms belonging to the inorganic framework except for the hydrogen atoms and the oxygen atoms involved in the P(1), P(2) and P(3) disorder systems.

After the refinement of both phases, two residual density maxima of approximately $\pm 3 \text{ e}^{-} \text{\AA}^{-3}$ were located near N(2). In compound **2**, there were also five other peaks located along the chain suggesting positional disorder of the organic template. Furthermore, in compound **1** two electron density peaks of ± 3.4 and $3.2 \text{ e}^{-} \text{\AA}^{-3}$ were found at the equatorial plane of the iron $[\text{M}(4)\text{O}_2\text{F}_2(\text{H}_2\text{O})_2]$ octahedron as well as a peak of around $\pm 2.3 \text{ e}^{-} \text{\AA}^{-3}$ at 1 Å from the P(4) atom. Such peaks located in the inorganic skeleton of **1** were also located in compound **2** but with significantly lower density values, around $\pm 1 \text{ e}^{-} \text{\AA}^{-3}$. In the case of compound **1**, such anomalies

are caused by the average structure resolution neglecting the satellite intensity due to the periodic character of the modulation.

Details of crystal data, data measurement and reduction, structure solution and refinement of the phases **1** and **2** are reported in Table 1. The selected bond distances and angles are reported in the ESI,† Tables S1 and S2. Structural drawings were made using the ATOMS 6.2,⁴² VESTA 3.1.7⁴² and TOPOS 4.0 programs.⁴³

Powder X-ray diffraction

X-ray powder diffraction for qualitative phase analysis of phase **3** using the Rietveld method with the FullProf program⁴⁴ was recorded using a Bruker D8 Advance Vario powder diffractometer equipped with a Cu tube, Ge(111) incident beam monochromator ($\text{Cu-K}_{\alpha 1} = 1.5406 \text{ \AA}$), and a Sol-X energy dispersive detector. The sample was mounted on a zero background silicon wafer embedded in a generic sample holder. Data were collected from 8 to $80^{\circ} 2\theta$ (step size = 0.02° and time per step = 90 s) at RT. Fixed divergence and anti-scattering slits giving a constant volume of sample illumination were used.

For the Rietveld refinement of **3**, obtained as a powdered sample, the structural model of **2** was used. The cobalt content was fixed to the amount calculated by the ICP-Q-MS analysis. The fitting of the profile parameters followed by refinement of the atomic coordinates and the atomic displacement parameters of the inorganic skeleton was performed. The organic template was not refined. Four different isotropic displacement parameters were refined: one for the iron and cobalt atoms and the remainder for the phosphorous, oxygen and fluorine atoms. Some soft constraints were included to have a chemically correct structural model.

Finally, all parameters (profile and structural) were refined simultaneously to obtain correct e.s.d.'s, obtaining good agreement between the experimental and the calculated diffractograms (Fig. S4†). Hence, the proposed chemical formula for **3** is $(\text{H}_4\text{baepn})_{0.5}[\text{Fe}^{\text{III}}_{2.0}\text{Fe}^{\text{II}}_{0.62}\text{Co}^{\text{II}}_{1.38}(\text{H}_2\text{O})_2(\text{HPO}_3)_{4-x}(\text{HPO}_4)_x\text{F}_4]$

Table 1 Crystallographic data and structure refinement parameters for phases **1** and **2** obtained by single crystal X-ray diffraction

Phase	1	2
Molecular weight (g mol ⁻¹)	744.05	747.53
Space group	<i>P</i> 2 ₁ / <i>c</i>	
<i>a</i> , <i>b</i> , <i>c</i> (Å)	13.6808(4) 12.6340(2) 12.7830(3) 116.983(4) 1968.94(8), 4 2.50(3), 2.51 0.231 × 0.094 × 0.052 1482	13.6823(4) 12.6063(3) 12.7535(4) 116.988(4) 1960.21(10), 4 2.51(3), 2.53 0.224 × 0.066 × 0.061 1480
β (°)		
<i>V</i> (Å ³), <i>Z</i>		
ρ_{obs} , ρ_{calc} (g cm ⁻³)		
Crystal size (mm)		
<i>F</i> (000)		
Diffractometer/temperature (K)	Agilent SuperNova (omega scan mode)/100(2)	
μ (mm ⁻¹), $T_{\text{min.}}/T_{\text{max.}}$	3.325, 0.694/0.865	3.499, 0.757/0.839
Radiation (Å)	$\lambda(\text{Mo K}\alpha) = 0.71073$	
Limiting indices <i>h</i> , <i>k</i> , <i>l</i>	-16 ≤ <i>h</i> ≤ 15 <i>k</i> ± 15 <i>l</i> ± 15 1.67–25.68, 99.8 13 887/3726/3670	<i>h</i> ± 16 <i>k</i> ± 15 <i>l</i> ± 15 1.67–25.68, 99.3 13 695/3700/3537
Theta range (°), completeness (%)		
No. of measured/independent/observed reflections	0.0189/0.016	0.0247/0.0212
<i>R</i> (int)/ <i>R</i> (sigma)	314/61	317/51
Parameters/restrictions	<i>R</i> ₁ = 0.0867 <i>wR</i> ₂ = 0.2067 <i>R</i> ₁ = 0.0873 <i>wR</i> ₂ = 0.2069 <i>x</i> = 0.0577 <i>y</i> = 95.4386 1.123	<i>R</i> ₁ = 0.0658 <i>wR</i> ₂ = 0.1384 <i>R</i> ₁ = 0.0676 <i>wR</i> ₂ = 0.1391 <i>x</i> = 0.0072 <i>y</i> = 62.0640 1.129
<i>R</i> [all data]	3.423, -1.658	3.08, -1.619
Weight factor		
G. O. F		
Max. and min. e. density (e Å ⁻³)		

($x \approx 0.38$), confirming the isostructurality between the three phases (see Tables S3 to S5† for the atomic coordinates and bond distances and angles of the Rietveld refinement of 3).

In addition, the pattern matching analysis of the diffraction patterns of the three compounds confirming the purity of the samples is given in the ESI† (Fig. S5).

Physicochemical characterization techniques

Thermogravimetric analyses were performed using an SDT 2960 simultaneous DSC-TGA TA instrument for **1** and using a Netzsch STA 449C one for **2** and **3**. Alumina crucibles containing around 20 mg of every sample were heated in air at a rate of 5 °C min⁻¹ from room temperature to 800 °C. Temperature dependence X-ray diffraction experiments for **1** and **3** were carried out in air using a Bruker D8 Advance diffractometer (Cu K α radiation) equipped with a variable-temperature stage (HTK2000), a Pt sample heater and a Vantec high-speed one dimensional detector with six degrees of angular aperture. The powder patterns were recorded in the 8 ≤ 2θ ≤ 38° range (step size = 0.033° and time per step = 0.4 s) at intervals of 15 °C, increasing the temperature at 10 °C min⁻¹ from room temperature to 810 °C. The IR spectra (KBr pellets) were obtained using a JASCO FT/IR-6100 spectrophotometer in the 400–4000 cm⁻¹ range. Diffuse reflectance spectra were measured at room temperature using a Varian Cary 5000 spectrophotometer in the 200–2500 nm range. X-ray photoelectron spectra of **1**, **2** and **3** were acquired using a SPECS (Berlin, Germany) system equipped with a

Phoibos 150 1D-DLD analyzer, monochromatic AlK α radiation (1486.6 eV, 300 W, 13 kV), and a multi-channel detector. Spectra were recorded in the constant pass energy mode at 80 eV for survey spectra and 30 eV for high resolution spectra, with an electron take-off angle of 90°. The spectrometer was previously calibrated using the Ag 3d_{5/2} line at 368.28 eV. The binding energy of the adventitious carbon (C1s) was set at 284.6 eV to correct sample charging. The spectra were fitted with the CasaXPS 2.3.16 software, which models the Gauss–Lorentzian contributions, after background subtraction (Shirley). Mössbauer spectra of **1**, **2** and **3** were obtained using a constant-acceleration Mössbauer spectrometer with a ⁵⁷Co/Rh source. Velocity calibration was done using a metallic Fe foil, and the Mössbauer spectral parameters are given relative to this standard at room temperature. The Mössbauer spectra were fitted with the NORMOS program.⁴⁵ Magnetic measurements on the powdered samples were performed in the temperature range 2.0–300 K for **1** and **3**, at 0.05, 0.2 and 1 T using a MPMS-7T SQUID magnetometer and a PPMS-system, both from Quantum Design. Heat capacity measurements for **1** and **3** were carried out by a standard two- τ relaxation method, using a PPMS-system, with magnetic fields up to 9 T and temperatures down to 2 K.

Results and discussion

Structure description

The asymmetric unit of **1** contains 35 non-hydrogen atoms, 29 of which belong to the host framework (four Fe, four P,

four F and seventeen O atoms) and the remaining 6 to the guest species (two N and four C atoms). Three of the oxygen atoms (O1', O2' and O3') present partial occupation as they belong to the hydrogen phosphate or phosphate groups which partially replace the phosphite units. All of the crystallographically independent atoms occupy general positions except for the C(4) atom which presents half site occupancy in order to generate the whole organic template. In 2 a total replacement of Fe(4) by Co(4) and a partial substitution of Fe(3) by Co(3) occurs in the M(3) and M(4) positions (Fig. S6†).

The average structure of compound 1 consists of a three-dimensional lattice formed by inorganic layers of iron(III) and iron(II) octahedra joined by the P(1) and P(2) phosphite groups (Fig. 2a).

These layers are linked between them through the P(3) and P(4) bridging HPO_3 units (Fig. 2b). The iron(III) octahedra $\text{Fe}(1)\text{O}_4\text{F}_2$ and $\text{Fe}(2)\text{O}_4\text{F}_2$ share oxygen vertices of the phosphorous pseudotetrahedra giving rise to [001] chains. These chains are joined along the [010] direction through the iron(II) octahedra dimers $\text{M}(3)\text{O}_4\text{F}_2$ and $\text{M}(4)\text{O}_2(\text{H}_2\text{O})_2\text{F}_2$, which share the O(18)–O(13) edges, leading to the layers which have eight-membered structural windows (Fig. 2a). These anionic layers stack along the [100] direction generating the open channels along the same direction, where the protonated templates are placed longitudinally (Fig. 2a and 3a), neutralizing the excess negative charge and stabilizing the inorganic building through hydrogen bonds (Fig. 3b).

The two types of iron(III) octahedra chains, the $[\text{Fe}(1)\text{O}_4\text{F}_2]$ octahedra linked together by the P(1) polyhedra and the $[\text{Fe}(2)\text{O}_4\text{F}_2]$ octahedra linked by the P(2) polyhedra, alternate in the [010] direction. Notice that the P(1)–H(1) and P(2)–H(2) bonds are in opposite directions. Moreover, it can be observed that the octahedra are linked between them through fluorine atoms along the *b* axis giving rise to an infinite $-\text{Fe}^{3+}\text{F}\text{--Fe}^{2+}\text{F}\text{--}$ linkage (Fig. 2a). The $\text{M}(4)\text{O}_2(\text{H}_2\text{O})_2\text{F}_2$ octahedron is not involved in the layer stacking because the two water molecules are coordinated at the apical positions roughly parallel to the stacking direction.

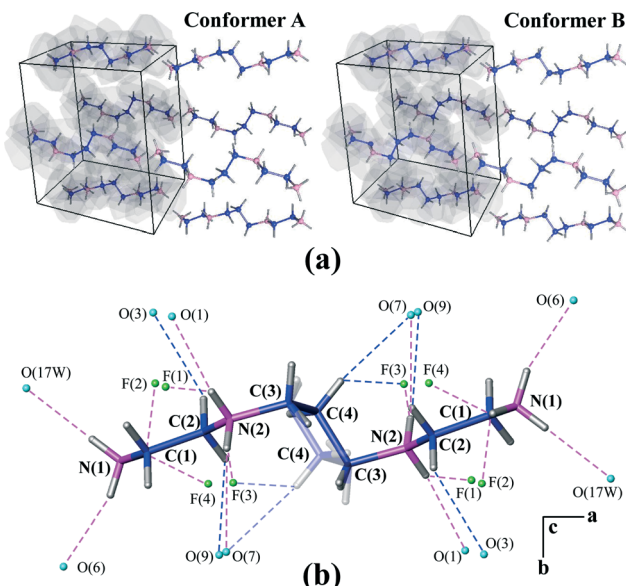


Fig. 3 a) VDP representation of the templates located in the voids of phase 1. b) The interlayer hydrogen bond scheme of phase 1.

In the $[\text{Fe}(1)\text{O}_4\text{F}_2]$ and $[\text{Fe}(2)\text{O}_4\text{F}_2]$ polyhedra the Fe–O bond lengths (1.938(8)–2.011(7) Å for 1 and 1.935(6)–2.000(6) Å for 2) as well as the Fe–F distances (1.929(7)–1.983(7) Å for 1 and 1.929(6)–1.993(4) Å for 2) are in good agreement with the 3+ oxidation state of the Fe(1) and Fe(2) atoms, based on the bond valence sum (BVS) calculations.⁴⁶ Both polyhedra display eight O–Fe–F and four O–Fe–O *cis* angles and two O–Fe–O and one F–Fe–F *trans* angles. However, in the $[\text{M}(3)\text{O}_4\text{F}_2]$ and $[\text{M}(4)\text{O}_2(\text{H}_2\text{O})_2\text{F}_2]$ octahedra, the M–O bond lengths span from 2.060(6) to 2.274(8) Å for 1 and from 2.056(4) to 2.216(6) Å for 2, and the M–F distances are in the range 1.996(6)–2.148(7) Å for 1 and 1.994(5)–2.125(5) Å for 2. In this case, the M–O/F distances indicate at first glance that, from the structural point of view, the M(3) and M(4) sites are in the 2+ state. In these polyhedra the fluorine atoms are located at the edges, giving rise to six O–M–F, five O–M–O

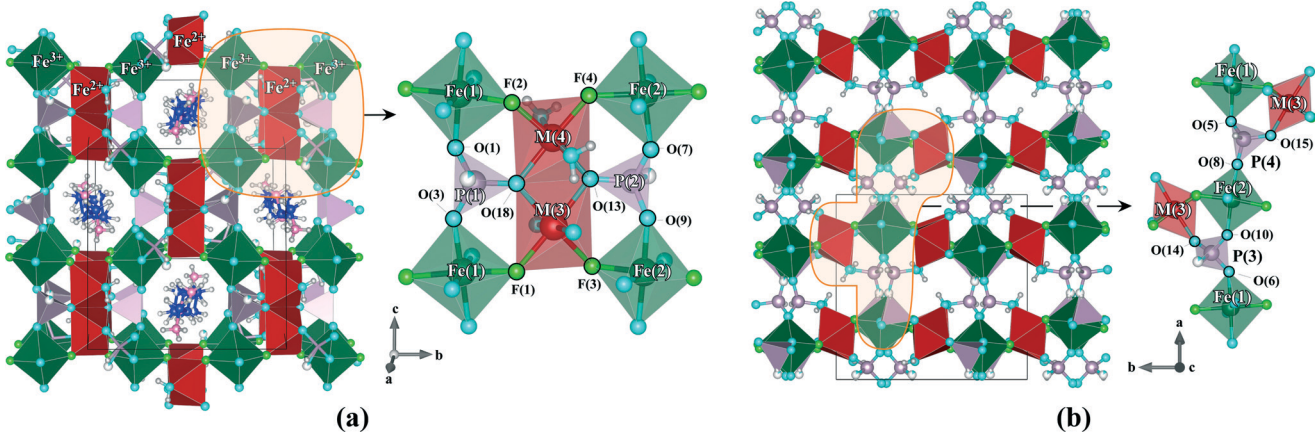


Fig. 2 a) Polyhedral representation of the 3D crystal structure of 1 viewed along the [100] direction. The shaded area shows a zoomed in view of the connectivity inside the inorganic layers. b) Layer stacking of P(3) and P(4) bridging units.

and one F–M–F *cis* angles and four O–M–O *cis* angles, and two O–M–F and one O–M–O *trans* angles.

The $S(O_h)$ values for phases **1** and **2**, calculated by continuous symmetry measure,⁴⁷ indicate more distorted octahedra for bivalent metals (M(3) and M(4)), however, they have very slight distortions with regard to the ideal octahedron.

The P–O distances of the $(HPO_3)^{2-}$ units are in the range 1.482(9)–1.544(8) Å for **1** and 1.493(7)–1.540(6) Å for **2**, and the P–H distances are 1.31(5) Å and 1.32(5) Å for **1** and **2**, respectively. The average O–P–O and H–P–O angles are around 112° and 107°, respectively, for both compounds, which are in the usual range for phosphite based compounds.⁴⁸ The terminal P(1)–O(1') bond distances are significantly greater than the rest of the P–O bonds (1.55(4) for **1** and 1.59(3) for **2**) which could be in good agreement with the existence of $(HPO_4)^{2-}$ groups as inferred from the electro-neutrality of the formula.

The phosphorus atoms make ten P–O–M (M = Fe, Co) linkages with minimum and maximum values for the P(2)–O(13)–Fe(3) and P(4)–O(8)–Fe(2) angles [123.3(4)° and 160.0(7)° for **1** and 123.5(3)° and 159.1(5)° for **2**].

The octahedra sharing a vertex display four M–F–M linkages with average angles of 127.5(3)° for **1** and 128.3(2)° for **2**. The M(3) and M(4) metals share an edge possessing two M–O–M linkages of around 98° and 100° for both phases.

Hydrogen bonding plays an important role in linking the tetramine cations to the framework (Fig. 3b). The terminal hydrogen-bond donor group, N(1), interacts with oxygens O(6) and O(17W) and the fluorine atoms F(2) and F(4) while the ‘internal’ donor group, N(2), interacts with O(1), O(7), F(1) and F(3). Three C–H···O and one C–H···F contacts are also present in the structures. The complete list of hydrogen bond interactions is shown in Table S6.[†]

In the Cambridge Structural Database (CSD) there are only three structures, based on ionic salts, containing uncomplexed *N,N'*-bis(2-aminoethyl)-1,3-propanediamine. In two of them, the molecule is a tetracation⁴⁹ and in the other, a trication,⁵⁰ with *gtttttg* (*g* indicates *gauche* and *t* *trans*) and *gttgggt* conformations, respectively. In the studied compounds, the existence of the symmetry centre forces the splitting of the central carbon (C4) into two positions producing conformers A and B with conformations not previously seen in the mentioned structures. Given the existence of torsion angles less than 30° and greater than 90° (see torsion angles in Tables S1 and S2[†]), the more systematic Klyne–Prelog system⁵¹ is required to describe them obtaining a *ttgaagt* conformation (*a* = anticlinal) for conformer A and a *ttsaastt* conformation (*s* = synperiplanar) for conformer B in both compounds.

The potential-free volume was estimated by the program PLATON,⁵² assuming that the templates could be removed from the channels, to be around 20% of the total volume for phases **1** and **2**. The volume occupied by these guest molecules was analyzed using the TOPOS 4.0 program⁴³ by means of Voronoi–Dirichlet polyhedra (VDP)⁵³ (Fig. 3a) and was found to be 23% of the crystal volumes. The matching percentage indicates the non-existence of accessible volume.

Thermal study

The TGA curves of **1**, **2** and **3** show three main weight losses. The results are given in the ESI[†] (Fig. S7). The first one (**1**, 80–285 °C; **2** and **3**, 80–275 °C) is associated with the release of two coordinated water molecules (~4.8%). Afterwards, there are two drops (**1**, 285–520 °C; **2** and **3**, 275 °C to 540 °C) related to the calcination of the organic molecule (~11.0%). The second process is marked by three and two exothermic peaks in the DTA (**1**, 285, 315 and 460 °C) and DSC (**2**, 269 and 287 °C; **3**, 272 and 292 °C) curves, respectively, due to the breakage of C–C and C–N bonds. The third process, which overlaps with the organic molecule decomposition, is assigned to the elimination of the fluoride anions. The two exothermic peaks observed in the DTA (**1**, 535 and 585 °C) and DSC curves (**2** and **3**, 545 and 565 °C) indicate the crystallization of the inorganic residues.

The thermodiffractometry in air of **1** and **3** reveal that their thermal stability limits are situated at 240 and 255 °C, respectively, under such experimental conditions (Fig. S8[†]). At these temperatures and as a consequence of the elimination of the two coordinated water molecules, the compounds become amorphous and, at 570 °C, the inorganic residues crystallize, in good agreement with the exothermic peaks observed in the DTA and DSC curves. The X-ray powder diffraction patterns of the residues obtained at 800 °C show the presence of $FePO_4$ [PDF file: 00-050-1635; S.G. $P3_{121}$ (152), $a = 5.048$ Å, $c = 11.215$ Å] for **1** and $FePO_4$ [PDF file: 01-084-0876; S.G. $P3_{121}$ (152), $a = 5.027$ Å, $c = 11.234$ Å] and $Co_3Fe_4(PO_4)_6$ [PDF file: 00-049-1083; S.G. $P\bar{1}$ (2), $a = 7.909$ Å, $b = 9.289$ Å, $c = 6.342$ Å, $\alpha = 108.48^\circ$, $\beta = 101.52^\circ$, $\gamma = 104.67^\circ$] for **3**. It is probable that the increase in weight observed during the TGA studies at around 450 °C is due to the oxidation of P(m) to P(v), resulting in the crystallization of the mentioned inorganic phosphates. The thermal evolution of the cell parameters for **1** and **3** was determined by pattern matching analysis (Fig. S9[†]). The volume of the phases exhibits a constant increase with thermal expansion coefficients of around 40×10^{-6} and $34 \times 10^{-6} \text{ }^\circ\text{C}^{-1}$ in the 30–195 °C temperature range.

Infrared, UV-Vis, XPS and Mössbauer spectroscopy

In the infrared spectra of the three compounds (Fig. S10[†]), the organic template is mainly represented by a group of overlapped maxima corresponding to stretching vibrations (ν) of the N–H and C–H bonds in the 3100–2500 cm^{-1} region. The $\delta(\text{NH}_3^+)$ band appears at 1600 cm^{-1} , indicating that the organic molecules are protonated and not coordinated to the inorganic building.

Regarding the inorganic part, at around 2400 cm^{-1} a narrow band splits in two, corresponding to the stretching vibrational mode of the P–H bond from the $(HPO_3)^{2-}$ groups, as can be observed in the spectra. At lower frequencies, in the 1100–400 cm^{-1} range, the bands corresponding to the P–O bond vibrations of the phosphite/phosphate groups are

observed. The $\nu(\text{O-H})$ absorption band related to the coordinated water molecules is also observed at around 3420 cm^{-1} .

The diffuse reflectance spectra of 1, 2 and 3 show mainly four bands (Fig. 4). In the diffuse reflectance spectrum of 1, two bands at approximately 10640 and 7520 cm^{-1} are observed. These bands are characteristic of the iron(II) d^6 -high spin cation in a slightly distorted octahedral environment and correspond to the electronic transitions from the $^5\text{T}_{2g}(^5\text{D})$ fundamental state to the excited level $^5\text{E}_{2g}(^5\text{D})$ that split as a consequence of the existence of the non-regular $[\text{M}(3)\text{O}_4\text{F}_2]$ and $[\text{M}(4)\text{O}_2(\text{H}_2\text{O})_2\text{F}_2]$ octahedra. The energy associated with this transition corresponds, according to the Tanabe-Sugano diagram,⁵⁴ to the Dq parameter. The value obtained is $Dq = 910\text{ cm}^{-1}$. An overlapped band situated at around 13510 cm^{-1} which corresponds to the forbidden transition from the $^6\text{A}_{1g}(^6\text{S})$ ground state to the $^4\text{T}_{1g}(^4\text{G})$ term is attributed to the presence of iron(III) d^5 -high spin configuration cations.⁵⁵ An intense band can also be observed at approximately 18180 cm^{-1} . This band likely corresponds to the intervalence transition between the Fe^{2+} and Fe^{3+} cations because their polyhedra share the four crystallographically independent fluorine atoms and the intermetallic bond distances are short enough (between 3.57 and 3.69 \AA).²⁷ In the spectra of compounds 2 and 3, distinguishing the transition bands characteristic of the Co^{2+} cations is not an easy task because of the overlapping of different d^5 , d^6 and d^7 high spin cation signals. However, these spectra show a significant change in the relative intensity of the split $^5\text{T}_{2g}(^5\text{D}) \rightarrow ^5\text{E}_{2g}(^5\text{D})$ transition bands as well as a reduction in the intensity of the $t_{2g}(\text{Fe}^{2+}) \rightarrow t_{2g}(\text{Fe}^{3+})$ intervalence transition, suggesting an effective substitution of Fe(II) by Co(II).

The chemical composition and the possible oxidation state of the iron and cobalt metals of the upper layers in these compounds were investigated by XPS measurements. The fitting together with the binding energies of the N 1s, P 2p, F 1s, Fe 2p and Co 2p_{1/2} peaks are deposited as ESI[†] (Fig. S11).

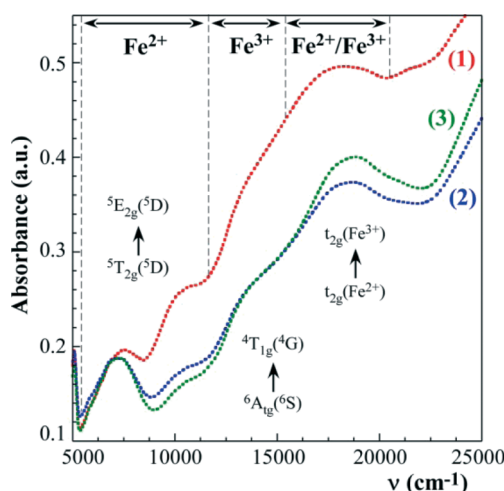


Fig. 4 UV-Vis spectra of iron(II)-iron(III) 1 (red) and cobalt(II)-substituted 2 (blue) and 3 (green) complexes.

The N 1s peaks are resolved into two peaks at around 399 and 401 eV which could be attributed to the existence of two primary and two secondary protonated amines per organic molecule. The P 2p peaks are deconvoluted into two doublets registered at binding energies between 130 and 133 eV and assigned to P(III) species, which used to be lower than those observed for P(V) species.⁵⁶ The F 1s peak centered at around 684 eV may be attributed to the metal-fluorine bonds.⁵⁷ The decomposition of Fe 2p_{3/2} spectra of compound 1 suggests the coexistence of Fe^{2+} close to 711 eV and Fe^{3+} at around 714 eV according to the values found for FeF_2 and FeF_3 fluorides, respectively.⁵⁸ Deconvolution of this region in compounds 2 and 3 is hindered by the interference of the Co LMM Auger line; however, the values of the Fe 2p_{1/2} component close to 724 and 727 eV , next to those found in 1, suggest also the mixed valency of the iron cations. Moreover, it is important to note the absence of the satellite peak of Fe 2p, which was previously reported for the mixed valence iron oxide Fe_3O_4 .⁵⁹ Likewise, compounds 2 and 3 show a Co 2p_{1/2} main line at a binding energy of around 797 eV , which is close to that found for a recently published cobalt(II) hybrid phosphite.⁶⁰ The presence of the strong satellite peak at around 6 eV from the Co 2p_{1/2} component is further evidence for Co^{2+} species.⁶¹

The powder ^{57}Fe room temperature Mössbauer spectra of the three compounds were studied as shown in Fig. 5. The best fit of 1, 2 and 3 leads to one doublet for iron(III) cations and another one for iron(II), obtaining $\text{Fe}^{3+}/\text{Fe}^{2+}$ area ratios of 1.35 , 2.80 and 3.20 , respectively. The values of the isomer shift and quadrupolar splitting parameters given in Table 2 show the characteristic values for the Fe^{3+} and Fe^{2+} cations. Given the multiplicity of the four crystallographically independent positions of the iron atoms and the metal-ligand distances obtained from the single-crystal structure analysis of compound 1, the Fe^{3+} cations are distributed over the positions Fe(1) and Fe(2) and the Fe^{2+} cations in the M(3) and M(4) positions. However, the percentage of Fe^{3+} exceeds 50% , so we infer that a partial substitution of Fe(II) by Fe(III) (Occ. = 0.296) occurs in the M(3) position (Fig. 6) as this presents a lower variation of the metal-ligand distances range than the $[\text{M}(4)\text{O}_2(\text{H}_2\text{O})_2\text{F}_2]$ octahedron.

Taking into account the structural features of compound 2, it is assumed that the Fe^{3+} ions occupy only the Fe(1) and Fe(2) positions. Therefore, considering the amount of cobalt obtained from the ICP-Q-MS analysis and the results from the structural refinement, the Fe^{2+} ions are totally replaced by Co^{2+} ions in the M(4) position and partially substituted in the M(3) position (Occ. = 0.290) (Fig. 6).

Magnetic behaviour of 1 and 3

Fig. 7 shows the temperature dependence of the molar magnetic susceptibility (χ_m) and inverse susceptibility ($1/\chi_m$) curves of compounds 1 and 3, measured on powdered samples from room temperature to 2 K in the Field Cooling (FC) mode at 2 kOe .

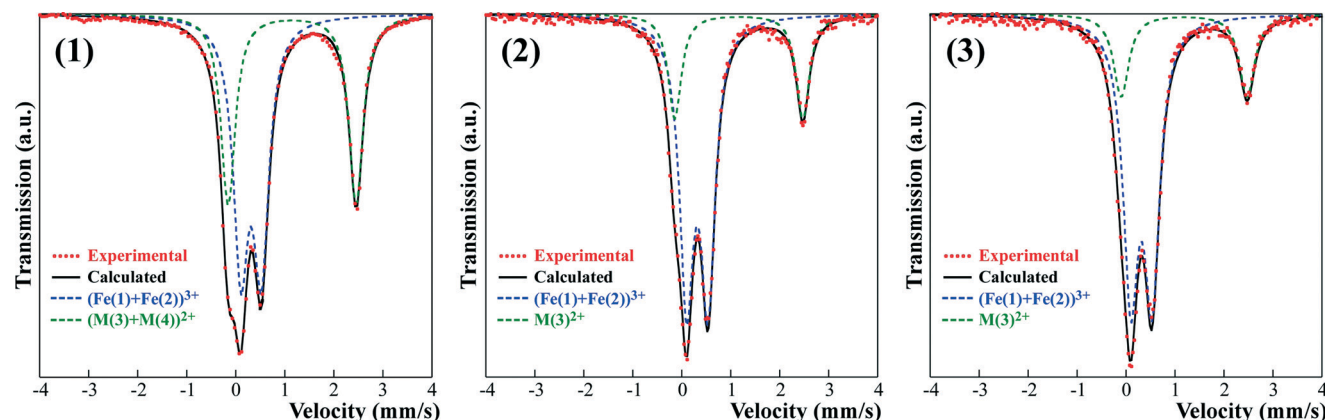


Fig. 5 Mössbauer spectra of **1**, **2** and **3** at room temperature.

Table 2 Hyperfine parameters at 298 K (δ : isomer shift; ΔE : quadrupolar splitting; %: proportion of each component) for **1**, **2** and **3**

	Position	δ (mm s ⁻¹)	ΔE (mm s ⁻¹)	(%)
1	(Fe(1) + Fe(2)) ³⁺	0.313(1)	0.42(1)	57.4
	(M(3) ^a + M(4)) ²⁺	1.150(1)	2.61(1)	42.6
2	(Fe(1) + Fe(2)) ³⁺	0.318(1)	0.44(1)	73.7
	M(3) ²⁺	1.165(1)	2.62(1)	26.3
3	(Fe(1) + Fe(2)) ³⁺	0.314(1)	0.44(1)	76.2
	M(3) ²⁺	1.187(1)	2.57(1)	23.8

^a M(3) position: 70.4% Fe²⁺/29.6% Fe³⁺.

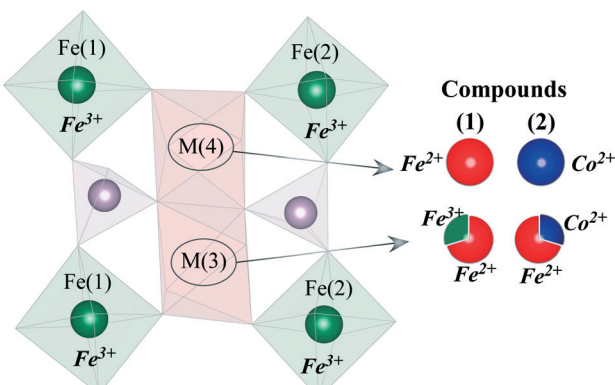


Fig. 6 Distribution of the Fe³⁺, Fe²⁺ and Co²⁺ cations inferred from the structural analysis and the Mössbauer study.

The molar magnetic susceptibility of **1** and **3** continuously increases as temperature decreases, showing a typical paramagnetic behaviour above 40 K. At lower temperatures, the χ_m curve of **1** reaches a width rounded maximum at approximately 28 K, showing a minimum at 20 K and then increases again with an inflection point close to 6 K. A similar behaviour was observed in compound $\text{Co}_2(\text{OH})\text{AsO}_4$.⁶² However, the behaviour of **3** at low temperatures is somewhat different in that the maximum which the FC curve displays at 28 K is quite sharp and that the susceptibility decreases much more than **1** after the maximum, reaching a minimum at approximately 10 K. Then, the χ_m curve increases until 2 K without

changes in the curvature. These behaviours at low temperature do not correspond to that of either a typical ferromagnet or antiferromagnet, although it looks more like that observed in antiferromagnets, especially in **3**.

The experimental data in both cases follow the Curie-Weiss law above 100 K (see lower insets in Fig. 7), allowing for the calculation of the Weiss temperature (**1**, $\theta = -95.6$ K and **3**, $\theta = -125$ K) and the average effective paramagnetic moment per metal ion (**1**, $\mu_{\text{eff}} = 5.60 \mu_B$ and **3**, $\mu_{\text{eff}} = 5.95 \mu_B$). The value of μ_{eff} for **1** is intermediate between the expected for Fe²⁺ ($5.4 \mu_B$) and Fe³⁺ ($5.9 \mu_B$), whereas that for the cobalt-substituted compound is slightly higher than that expected for Fe³⁺, probably because the Co ions present an extra contribution coming from the angular momentum. The negative Weiss temperatures together with the decrease of the $\chi_m T$ products with decreasing temperature indicate that the main magnetic interactions in these compounds are antiferromagnetic. The abrupt increase of the susceptibility below 20 K for **1** and the sharp maximum close to 28 K for **3** correspond to the onset of AF order, as will be described later from the $M(H)$ curves and heat capacity (C_p) data.

The upper insets of Fig. 7 show the low temperature ZFC and FC molar susceptibility (χ_m) details at 0.5, 2 and 10 kOe. For **1** a small irreversibility appears at 0.5 kOe below 30 K and, although it practically disappears at fields higher than 2 kOe, a tiny contribution persists at up to 10 kOe. For **3** a small splitting of the curves can also be observed but its intensity is much less dependent on the magnetic field than in compound **1**. Moreover, the minimum location is reliant on the magnetic field, shifting from 9 to 16 K upon increasing the field from 0.5 to 10 kOe for **3**, while for **1** the position remains practically unchanged at 20 K regardless of the applied field. The existence of irreversibility can only be attributed to the existence of a weak ferromagnetic component.

Fig. 8a depicts the field dependence of the magnetization of **1** at different temperatures. At 2 K, the magnetization increases almost linearly with the magnetic field until a critical field of 45 kOe, where a metamagnetic transition occurs. The magnetization value ($0.45 \mu_B/\text{Fe ion}$) obtained at the highest applied field, 90 kOe, is far from the theoretical saturation for

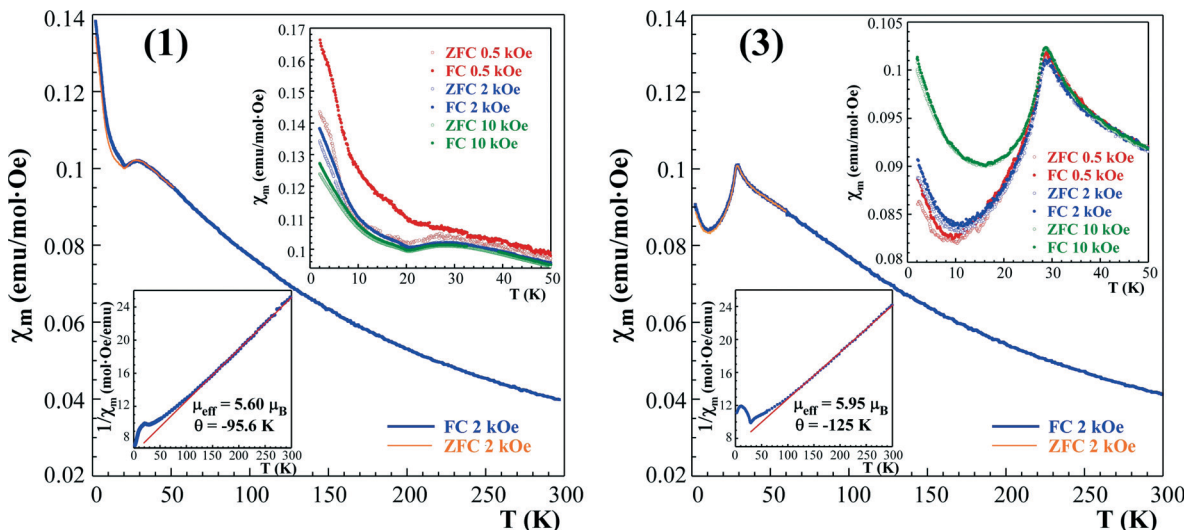


Fig. 7 Temperature dependence of χ_m for compounds **1** and **3** measured under 2 kOe. The lower inset shows the $1/\chi_m$ curve fitted to the Curie-Weiss law and the upper inset the enlargement of the low-temperature region of ZFC-FC data measured under 0.5, 2 and 10 kOe.

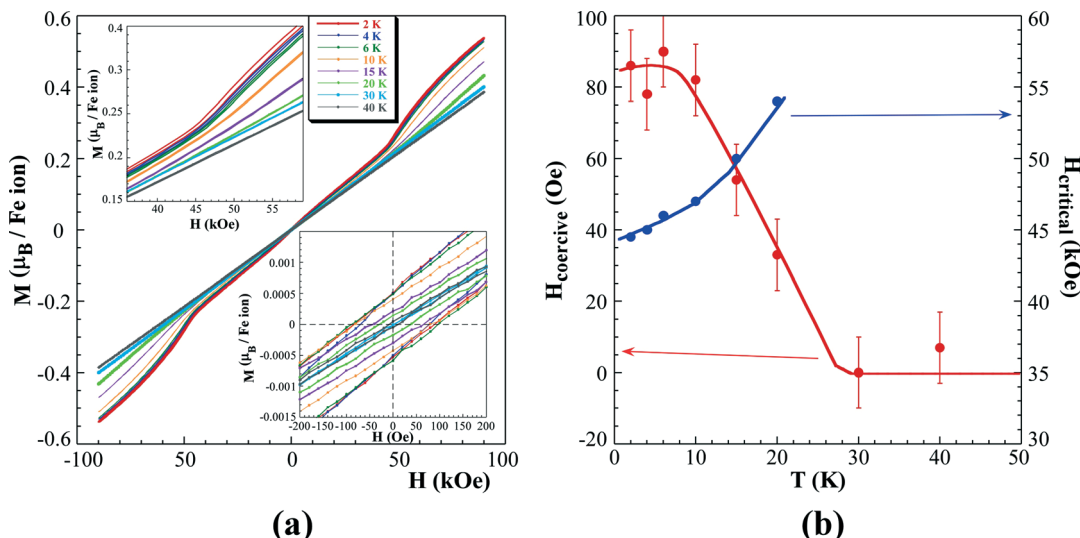


Fig. 8 a) Magnetization vs. applied magnetic field at different temperatures for **1**. The upper inset shows the details of the metamagnetic transition and the lower inset the enlargement of the small coercivity of the hysteresis loops. b) Thermal evolution of the coercive field of the hysteresis loops and the critical field of the metamagnetic transition.

the Fe(II) ($4 \mu_B$) and Fe(III) ($5 \mu_B$) ions, indicating the existence of a strong magnetocrystalline anisotropy. Despite the $M(H)$ general behaviour being characteristic of antiferromagnetic order, it is important to note the existence of a small hysteresis with a coercive field of 85 Oe at low temperatures, which confirms the existence of a weak ferromagnetic component (lower inset in Fig. 8a).

The hysteresis decreased as the temperature increased, disappearing in the paramagnetic region. The temperature increase also resulted in a positive shift of the critical field of the metamagnetic transition (upper inset in Fig. 8a). Above 20 K, the metamagnetic transition disappeared and the $M(H)$ curves were completely linear up to 90 kOe (Fig. 8b). In the case of compound **3**, the hysteresis loops did not show any

significant remnant magnetization. However, there was also a critical field close to 62 kOe at 2 K indicating the existence of a metamagnetic transition (Fig. S12, ESI†).

To get further insight into the weak ferromagnetic component of **1**, we measured the thermoremanent magnetization (TRM) as well as the ac magnetic susceptibility. The TRM curve was measured at $H = 0$ after cooling from $T \geq T_N$ under a magnetic field of 5 kOe. As can be observed in Fig. S13,† the value decreased continuously with the increase in temperature, reaching zero above the Neel temperature. The appearance of positive remanent magnetization below T_N confirms the existence of a weak ferromagnetic component. In addition, it is important to note the appearance of a clear shoulder at around 6 K as was also pointed out in the FC curve.

The real (χ') and imaginary (χ'') components of the ac susceptibility at 1000 Hz with an ac field of 10 Oe are shown in Fig. S14.[†] χ' shows a broad maximum centred at 28 K (T_N) whereas χ'' , which should be zero in antiferromagnetic compounds, has a small contribution associated with the weak ferromagnetic component. Surprisingly a sharp peak emerges in both χ' and χ'' at around 4.5 K indicating the presence of a magnetic transition of different nature from the previous one. This transition was masked in the magnetic susceptibility by the weak ferromagnetic component but should be the responsible for the shoulder observed at around 6 K in the FC and TMR curves. To check the origin of this low temperature transition we measured the ac susceptibility at different frequencies (inset of Fig. S14[†]). The peak height decreased and the position of the maximum shifted to higher temperatures with increasing frequency, as is usual in spin glass transitions. The spin glass nature of the transition is further confirmed by the absence of any anomaly at 4.5 K in the heat capacity data. The coexistence of antiferromagnetism and spin glass behaviours was previously observed in other insulator materials.^{23,63} This result could be due to the simultaneous but random presence of Fe(II) and Fe(III) cations in the M(3) position of compound **1** (Fig. 6), giving rise to the competing interactions. Both randomness and competing interactions lead to spin frustration, ultimately resulting in the spin-glass state.

Considering the structural features of compounds **1** and **2**, studied by single crystal X-ray diffraction, and taking into account that **3** is isotopic, several magnetic pathways can take place in these three phases. Inside the layers the metal–metal distances range from 3.2 to 3.7 Å; consequently, direct interactions are not negligible. A view of the most important magnetic exchange interactions M–O–M and M–F–M in **1** and **2** is given in Fig. S15.[†] The J_1 pathway represents direct intradimeric magnetic interactions *via* oxygen atoms between the

$\text{M}(3)\text{O}_4\text{F}_2$ and $\text{M}(4)\text{O}_2(\text{H}_2\text{O})_2\text{F}_2$ polyhedra. The values of the bond angles for J_1 are around 98° and 100° , which could lead to a ferromagnetic interaction inside the dimers. However, J_2 to J_5 pathways imply superexchange interactions through fluorine atoms involving bond angles between approximately 124 and 133° and clearly indicate the existence of an antiferromagnetic coupling. The superexchange inter- and intralayer M–O–P–O–M interactions allow one to propagate the magnetic interactions giving rise to a three-dimensional magnetic system. The bond distances and angle values for the exchange pathways are very close for **1** and the cobalt substituted compounds **2** and **3**. Hence, the differences in the magnetic properties of **1**–**3** cannot be explained from a structural point of view.

Taking into account that the Co^{2+} ions prefer the $\text{M}(3)\text{O}_4\text{F}_2$ and $\text{M}(4)\text{O}_2(\text{H}_2\text{O})_2\text{F}_2$ octahedra, the substitution of Fe(II) (d^6) ($S = 2$) by Co(d^7) ($S = 3/2$) in the framework of **1** modifies the nature of some magnetic interactions involving the J_1 pathway.

The specific heat curves presented in Fig. 9 show a small maximum centered at 20.5 K for **1** and a sharp magnetic peak at 28 K for **3**. Despite the anomaly observed for **1** not having the typical appearance of a λ -type second-order transition peak as in the case of the cobalt containing compound, it can be associated with the establishment of a three-dimensional antiferromagnetic order in good agreement with the magnetic susceptibility data. It is important to note the absence of any additional anomaly at low temperatures, confirming the spin glass nature of the transition observed in the ac susceptibility at 4.5 K. The continuous increase of C_p at higher temperatures is due to the lattice contribution (C_{pho}), which does not show any tendency to saturation. In fact, the C_p values at 300 K for both compounds are around $660 \text{ J mol}^{-1} \text{ K}^{-1}$, still far from the expected values (**1**: $1287.8 \text{ J mol}^{-1} \text{ K}^{-1}$ and **3**: $1294.0 \text{ J mol}^{-1} \text{ K}^{-1}$) according to

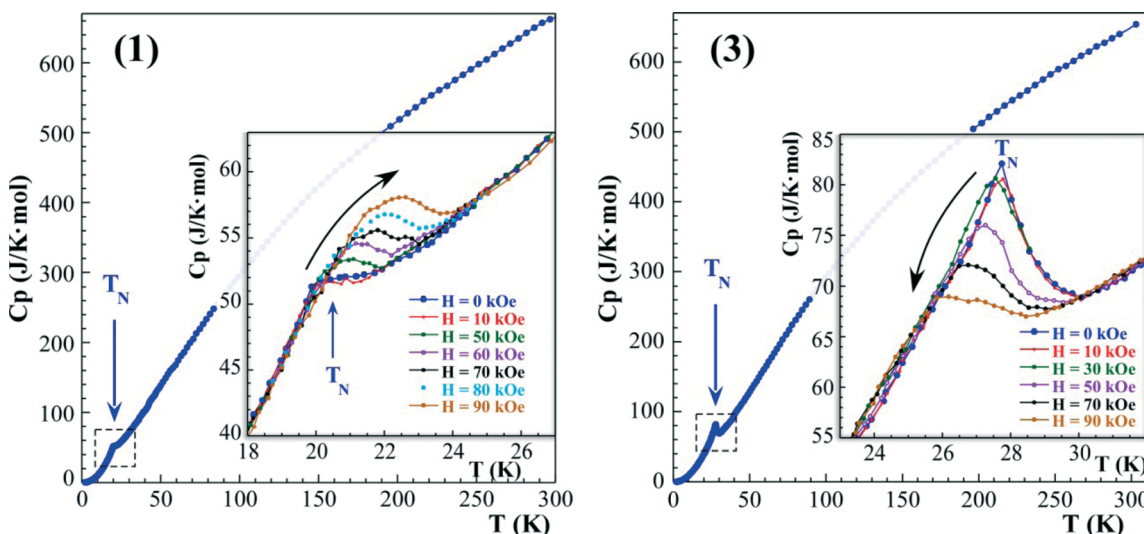


Fig. 9 Specific heat of compounds **1** and **3** between 2 and 300 K. The insets show the enlargement around the Neel temperature as a function of temperature in the presence of external magnetic fields, H , in the 0–90 kOe range.

the Dulong and Petit law (51.6 and 51.9 ions per unit formula for **1** and **3**, respectively). This is due to the presence of light atoms with very high excitation energy.

In order to extract the magnetic contribution, C_{mag} , C_{pho} was estimated using the Debye model and by considering the existence of three Debye temperatures (the minimum number of free parameters that will allow us to fit the experimental data). In this way, if the number of atoms in the unit cell is N , we suppose n_1 atoms with a Debye temperature θ_{D1} , n_2 atoms with a Debye temperature θ_{D2} , and $n_3 = (N - n_1 - n_2)$ atoms with a Debye temperature θ_{D3} . Therefore, there are five free parameters, namely n_1 , n_2 , θ_{D1} , θ_{D2} , and θ_{D3} . This approach has been used successfully in previous studies of other hybrid compounds.⁶⁴ The best fittings obtained were: $n_1 = 10.2$, $\theta_{D1} = 213$ K, $n_2 = 15.6$, $\theta_{D2} = 650$ K and $\theta_{D3} = 2350$ K for compound **1** ($N = 51.6$) and $n_1 = 10.9$, $\theta_{D1} = 232$ K, $n_2 = 15.6$, $\theta_{D2} = 689$ K and $\theta_{D3} = 2578$ K for compound **3** ($N = 51.9$). The good quality of the fits (see the continuous lines in Fig. S16†) allows us to consider that this phenomenological model determines reasonably well the phonon contribution. The magnetic contribution, obtained as $C_{\text{mag}} = C_p - C_{\text{pho}}$, is plotted in the insets of Fig. S16(a) and (b)† for compounds **1** and **3**, respectively. The value of C_{mag} in the maximum is clearly greater for **3**, $46.5 \text{ J mol}^{-1} \text{ K}^{-1}$, than for **1**, $34.5 \text{ J mol}^{-1} \text{ K}^{-1}$. In addition, whereas in **3** C_{mag} has a λ -peak shape, in **1**, C_{mag} has a triangular shape, extending up to 60 K. These findings also indicate that compound **1** has a more complex magnetic structure than compound **3**.

Heat capacity was also studied in the presence of several magnetic fields. With increasing magnetic field in **3**, the sharp λ -type magnetic peak became more rounded and shifted to lower temperatures, which is in good agreement with a global antiferromagnetic behaviour as was also observed from the magnetic susceptibility. In the case of compound **1**, an unexpected behaviour was observed. The small maximum shifted to higher temperatures, increased with the magnetic field and became better defined. Usually, the effect of the magnetic field on ferromagnetic transitions consists of shifting the λ anomaly to higher temperatures, making it more rounded and smaller in height.

Therefore, the small value of the anomaly observed in **1** could be associated with an incommensurate magnetic structure, in which the entropy difference with the paramagnetic state is lower than in commensurate structures. The proposal of this kind of structure is also supported by the behaviour of the anomaly under the applied magnetic field. A similar behaviour of the specific heat anomaly was observed in compound $\text{Co}_2(\text{OH})\text{AsO}_4$ ⁶² and in that case it was interpreted as an evolution of the magnetic structure to commensurability.

Conclusions

The mild hydrothermal technique was used for the synthesis of three novel 3D open-framework fluorinated mixed valence $\text{Fe}(\text{II})\text{--Fe}(\text{III})$ phosphites with channels templated by

protonated tetramine chains. The combined information from chemical analysis, X-ray diffraction and Mössbauer spectroscopy allowed us to determine the Fe^{3+} , Fe^{2+} and Co^{2+} cation distribution over the four metal sites. While $\text{Fe}(1)$ and $\text{Fe}(2)$ positions have a full occupancy of Fe^{3+} in the three phases, $\text{M}(4)$ is occupied by Fe^{2+} in **1** but totally replaced by Co^{2+} in **2** and **3**. The $\text{M}(3)$ position presents partial occupations: $0.30 \text{ Fe}^{3+} : 0.70 \text{ Fe}^{2+}$ for **1**, $0.29 \text{ Co}^{2+} : 0.71 \text{ Fe}^{2+}$ for **2** and $0.38 \text{ Co}^{2+} : 0.62 \text{ Fe}^{2+}$ for **3**.

The average structure resolution of **1** shows, ignoring the satellite intensity, electron density peaks above $\pm 3 \text{ e}^{-} \text{ \AA}^{-3}$ which are found at the equatorial plane of the $[\text{M}(4)\text{O}_2\text{F}_2(\text{H}_2\text{O})_2]$ octahedron and near the nitrogen $\text{N}(2)$ atom belonging to the organic template. The reciprocal analysis of **1** shows satellite reflections, described by $q = 0.284(2)a^*$, which are the result of an incommensurate long-range order involving the crystallographic [100] direction. It is logical to think that the incommensurate structure is related to an incommensurate disorder of the organic molecule located along the [100] channels within the inorganic framework. This long-range order of the template seems to affect also the inorganic skeleton because of the extensive network of hydrogen bonds, as was deduced from the residual electron densities located near the $\text{M}(4)$ and $\text{P}(4)$ sites. This incommensurability is not observed in **2**. Therefore, while the template movement along the a axis describes a structural modulation of the structure of **1**, in **2** it does not have a periodic character and only local disorders were observed.

Magnetic measurements of **1** and **3** are consistent with the existence of major antiferromagnetic interactions. Compound **1** also exhibits weak ferromagnetism at low temperature and an additional spin glass transition at the freezing temperature $T_f = 4.5$ K. Far from the expected increase in random magnetic interactions with Co substitution because of its anisotropic nature, the spin glass transition and the weak ferromagnetism disappears in compound **3**. So, the presence of $\text{Co}(\text{II})$ ions in both $\text{M}(3)$ and $\text{M}(4)$ sites and in particular the suppression of the random mixed valency of the iron cations in $\text{M}(3)$ site can reduce drastically the magnetic frustration.

Specific heat curves show a small anomaly at 20.5 K for **1** and a sharp magnetic peak at 28 K for **3**. Strikingly, the anomaly observed in **1** increases with the magnetic field and becomes better defined. Characteristics such as the low value of the anomaly and its behaviour under the applied magnetic field suggest that this is due to the existence of an incommensurate magnetic structure as was interpreted in compound $\text{Co}_2(\text{OH})\text{AsO}_4$. In fact, the existence of residual electron density peaks located in the $\text{M}(4)$ site, occupied by $\text{Fe}(\text{II})$ cations, seems to have some kind of relationship with the incommensurate magnetic structure of **1**. In addition, the specific heat study of the cobalt-substituted phase **3** does not show signs of the existence of an incommensurate magnetic structure at low temperatures. It should be recalled that the $\text{M}(4)$ site is totally occupied by $\text{Co}(\text{II})$ ions in phases **2** and **3** and does not show significant residual maxima as was observed in the structural study of **2**.

Acknowledgements

This work was financially supported by the “Ministerio de Ciencia e Innovación” (MAT2010-15375 and MAT2011-27573-C04), the “Gobierno Vasco” (IT630-13) and the “UPV/EHU” (UFI11/15), which we gratefully acknowledge. The authors thank the technicians of SGIker (UPV/EHU), financed by the National Program for the Promotion of Human Resources within the National Plan of Scientific Research, Development and Innovation, “Ministerio de Ciencia y Educación” and “Fondo Social Europeo” (FSE), for the X-ray diffraction, XPS, chemical and spectroscopic measurements. J. Orive wishes to thank the Universidad del País Vasco, UPV/EHU for funding.

Notes and references

- 1 D. MasPOCH, D. Ruíz-Molina and J. Veciana, *Chem. Soc. Rev.*, 2007, **36**, 770.
- 2 S. Natarajan and S. Mandal, *Angew. Chem., Int. Ed.*, 2008, **47**, 4798.
- 3 M. E. Davis, *Nature*, 2002, **417**, 813; E. R. Parnham and R. E. Morris, *Acc. Chem. Res.*, 2007, **40**, 1005; J. Jiang, J. Yu and A. Corma, *Angew. Chem., Int. Ed.*, 2010, **49**, 3120.
- 4 J. Yu and R. Xu, *Acc. Chem. Res.*, 2010, **43**(9), 1195.
- 5 T. Loiseau and G. Férey, *J. Mater. Chem.*, 1996, **6**, 1073; C. Sasseoye, J. Marrot, T. Loiseau and G. Férey, *Chem. Mater.*, 2002, **14**, 1340.
- 6 J. Orive, E. S. Larrea, R. Fernández de Luis, M. Iglesias, J. L. Mesa, T. Rojo and M. I. Arriortua, *Dalton Trans.*, 2013, **42**, 4500; H.-L. Huang and S.-L. Wang, *Chem. Commun.*, 2010, **46**, 6141.
- 7 Y. Yang, N. Li, H. Song, H. Wang, W. Chen and S. Xiang, *Chem. Mater.*, 2007, **19**, 1889; J. Li, L. Li, J. Liang, P. Chen, J. Yu, Y. Xu and R. Xu, *Cryst. Growth Des.*, 2008, **8**(7), 2318; J. Liang, J. Li, J. Yu, P. Chen, Q. Fang, F. Sun and R. Xu, *Angew. Chem., Int. Ed.*, 2006, **45**, 2546.
- 8 R. Chao, Y. Kong, L. Jin, Y. Ren, Y. Ding, N. Li, N. Guan and S. Xiang, *Microporous Mesoporous Mater.*, 2013, **176**, 132.
- 9 H.-Y. Lin, C.-Y. Chin, H.-L. Huang, W.-Y. Huang, M.-J. Sie, L.-H. Huang, Y.-H. Lee, C.-H. Lin, K.-H. Lii, X. Bu and S.-L. Wang, *Science*, 2013, **339**, 811.
- 10 P. Feng, X. Bu and G. D. Stucky, *Nature*, 1997, **388**, 735; X. Bu, P. Feng and G. D. Stucky, *J. Am. Chem. Soc.*, 1998, **120**, 11204.
- 11 A. Choudhury, S. Natarajan and C. N. R. Rao, *Inorg. Chem.*, 2000, **39**, 4295.
- 12 S. Natarajan, *Chem. Commun.*, 2002, 780.
- 13 J. A. Rodgers and W. T. A. Harrison, *J. Mater. Chem.*, 2000, **10**, 2853.
- 14 W.-M. Chang, M.-Y. Cheng, Y.-C. Liao, M.-C. Chang and S.-L. Wang, *Chem. Mater.*, 2007, **19**, 6114.
- 15 M. E. Davis and R. F. Lobo, *Chem. Mater.*, 1992, **4**, 756.
- 16 D. W. Lewis, D. J. Wilcock and C. R. A. Catlow, *Nature*, 1996, **382**, 604; J. Li, J. Yu and R. Xu, *Microporous Mesoporous Mater.*, 2007, **101**, 406; R. Pophale, F. Daeyaert and M. W. Deem, *J. Mater. Chem. A*, 2013, **1**, 6750.
- 17 A. Lu, N. Li, Y. Ma, H. Song, D. Li, N. Guan, H. Wang and S. Xiang, *Cryst. Growth Des.*, 2008, **8**(7), 2377.
- 18 A. Lakiss, A. Simon-Masseron, F. Porcher, S. Rigolet and J. Patarin, *Eur. J. Inorg. Chem.*, 2007, **25**, 4043; X. Luo, D. Luo, M. Gong, Y. Chen and Z. E. Lin, *CrystEngComm*, 2011, **13**, 3646; L. Xue, D. Luo, X. Luo, H. Zeng and Z. Lin, *Solid State Sci.*, 2013, **19**, 80.
- 19 G.-M. Wang, J.-Q. Jiao, X. Zhang, X.-M. Zhao, X. Yin, Z.-H. Wang, Y.-X. Wang and J.-H. Lin, *Inorg. Chem. Commun.*, 2014, **39**, 94; L.-M. Li, K. Cheng, F. Wang and J. Zhang, *Inorg. Chem.*, 2013, **52**(10), 5654; G. Wang, J. Li, X. Zhang, P. Wang, B. Pang, Z. Wang, Y. Wang, J. Lin and C. Pan, *Dalton Trans.*, 2013, **42**, 13084.
- 20 T. Rojo, J. L. Mesa, J. Lago, B. Bazán, J. L. Pizarro and M. I. Arriortua, *J. Mater. Chem.*, 2009, **19**, 3793.
- 21 W. Yang, J. Li, Q. Pan, H. Xing, Y. Chen, J. Yu and R. Xu, *J. Mater. Chem.*, 2009, **19**, 4523; S. Mandal, S. Natarajan, J. M. Grenèche, M. Riou-Cavellec and G. Férey, *Chem. Mater.*, 2002, **14**, 3751.
- 22 G. Paul, A. Choudhury, E. V. Sampathkumaran and C. N. R. Rao, *Angew. Chem., Int. Ed.*, 2002, **41**(22), 4297.
- 23 U.-C. Chung, J. L. Mesa, J. L. Pizarro, I. de Meatz, M. Bengoechea, J. Rodríguez Fernández, M. I. Arriortua and T. Rojo, *Chem. Mater.*, 2011, **23**, 4317.
- 24 B. Bazan, J. L. Mesa, J. L. Pizarro, A. Peña, M. I. Arriortua and T. Rojo, *Z. Anorg. Allg. Chem.*, 2005, **631**, 2026.
- 25 J. Orive, J. L. Mesa, E. Legarra, F. Plazaola, M. I. Arriortua and T. Rojo, *J. Solid State Chem.*, 2009, **182**, 2191.
- 26 Y. Fan, T. Song, G. Li, Z. Shi, G. Yu, J. Xu and S. Feng, *Inorg. Chem. Commun.*, 2005, **8**(8), 661.
- 27 S. Fernández-Armas, J. L. Mesa, J. L. Pizarro, M. I. Arriortua and T. Rojo, *Mater. Res. Bull.*, 2007, **42**(3), 544.
- 28 S. Fernández-Armas, J. L. Mesa, J. L. Pizarro, J. S. Garitaonandia, M. I. Arriortua and T. Rojo, *Angew. Chem., Int. Ed.*, 2004, **43**(8), 977.
- 29 F. Shiba, R. Fujishiro, T. Kojima and Y. Okawa, *J. Phys. Chem. C*, 2012, **116**, 3394.
- 30 Q. Lin, C. Lei, G. Tang, Q. Zhang and Y. He, *Hyperfine Interact.*, 2013, **219**, 95; E. Coronado, J. R. Galán-Mascarós, C. J. Gómez-García and V. Laukhin, *Nature*, 2000, **408**, 447.
- 31 O. Sato, T. Iyoda, A. Fujishima and K. Hashimoto, *Science*, 1996, **172**, 704.
- 32 J.-H. Park, E. Izmár, M. W. Meisel, Y.-D. Huh, F. Frye, S. Lane and D. R. Talham, *Appl. Phys. Lett.*, 2004, **85**, 3797; J.-H. Park, F. Frye, S. Lane, E. Izmár, Y.-D. Huh, D. R. Talham and M. W. Meisel, *Polyhedron*, 2005, **24**, 2355.
- 33 T. Liu, Y.-J. Zhang, S. Kanegawa and O. Sato, *J. Am. Chem. Soc.*, 2010, **132**, 8250; S. Gawali-Salunke, F. Varret, I. Maurin, C. Enachescu, M. Malarova, K. Boukheddaden, E. Codjovi, H. Tokoro, S. Ohkoshi and K. Hashimoto, *J. Phys. Chem. B*, 2005, **109**, 8251; N. Shimamoto, S. Ohkoshi, O. Sato and K. Hashimoto, *Inorg. Chem.*, 2002, **41**, 678; A. Goujon, F. Varret, V. Escaux, A. Bleuzen and M. Verdaguer, *Polyhedron*, 2001, **20**, 1339.
- 34 H.-M. Hu, X.-Y. Huang, H.-S. Sun, D.-L. Long, J.-S. Huang and X.-Z. You, *J. Coord. Chem.*, 1999, **47**, 531; I. P.-Y. Shek,

W.-F. Yeung, T.-C. Lau, J. Zhang, S. Gao, L. Szeto and W.-T. Wong, *Eur. J. Inorg. Chem.*, 2005, 364; J.-E. Koo, D.-H. Kim, Y.-S. Kim and Y. Do, *Inorg. Chem.*, 2003, 42, 2983; A. Escuer, R. Vicente, M. S. El Fallah, X. Solans and M. Font-Bardia, *Inorg. Chim. Acta*, 1996, 247, 85; R. Vicente, A. Escuer, J. Ribas, M. S. El Fallah, X. Solans and M. Font-Bardia, *Inorg. Chem.*, 1993, 32, 1920.

35 J. Qiao, L. Zhang, Y. Yu, G. Li, T. Jiang, Q. Huo and Y. Liu, *J. Solid State Chem.*, 2009, 182, 1929.

36 W. Yingua, *J. Appl. Crystallogr.*, 1987, 20, 258.

37 A. C. T. North, D. C. Phillips and F. S. Mathews, *Acta Crystallogr., Sect. A: Cryst. Phys., Diffraction, Theor. Gen. Crystallogr.*, 1968, 24, 351.

38 *CrysAlisPro CCD and RED*, version 171.35.19, Oxford Diffraction, Ltd., Oxford, U.K., 2011.

39 G. M. Sheldrick, *SHELXS 97: Program for the Solution of Crystal Structures*, University of Göttingen, Germany, 1977.

40 G. M. Sheldrick, *SHELXL 97: Program for the Refinement of Crystal Structures*, University of Göttingen, Germany, 1977.

41 L. J. Farrugia, *J. Appl. Crystallogr.*, 1999, 32, 837.

42 E. Dowty, *ATOMS: A Computer Program for Displaying Atomic Structures*, Shape Software, 512 Hidden Valley Road, Kingsport, TN, 1993; K. Momma and F. Izumi, *J. Appl. Crystallogr.*, 2008, 41, 653.

43 V. A. Blatov, *IUCr CompComm. Newslett.*, 2006, vol. 7, p. 4.

44 J. Rodríguez-Carvajal, *Rietveld Pattern Matching Analysis of Powder Patterns, FULLPROF*, 1994.

45 R. A. Brand, J. Lauer and D. M. Herlach, *J. Phys. F: Met. Phys.*, 1983, 13, 675.

46 I. D. Brown and D. Altermatt, *Acta Crystallogr., Sect. B: Struct. Sci.*, 1985, 41(4), 244.

47 S. Álvarez, D. Avnir, M. Llunel and M. Pinsky, *New J. Chem.*, 2002, 26, 996; M. Llunel, D. Casanova, J. Cirera, J. M. Bofill, P. Alemany, S. Álvarez, M. Pinsky and D. Yatimir, *SHAPE v1.1a: Program for Continuous Shape Measure Calculations of Polyhedral Xn and MLn Fragments*, 2003.

48 J. Loub, *Acta Crystallogr., Sect. B: Struct. Sci.*, 1991, 47(4), 468.

49 X.-C. Su, H.-K. Lin, S. R. Zhu, L.-H. Weng, X.-B. Leng and Y.-T. Chen, *Supramol. Chem.*, 2002, 14, 41; H. B. Szczesniak, V. Patroniak, W. Radecka-Paryzek and M. Kubicki, *Acta Crystallogr., Sect. C: Cryst. Struct. Commun.*, 2009, 65, 371.

50 V. Patroniak, W. Radecka-Paryzek and M. Kubicki, *Acta Crystallogr., Sect. C: Cryst. Struct. Commun.*, 2008, 64, 511.

51 E. V. Anslyn and D. A. Dougherty, *Modern Physical Organic Chemistry*, University Science Books, 2006.

52 A. L. Spek, *J. Appl. Crystallogr.*, 2003, 36, 7; A. L. Spek, *Acta Crystallogr., Sect. D: Biol. Crystallogr.*, 2009, 65, 148.

53 M. O'Keeffe, *Acta Crystallogr., Sect. A: Cryst. Phys., Diffraction, Theor. Gen. Crystallogr.*, 1979, 35, 772; V. A. Blatov, A. P. Shevchenko and V. N. Serezhkin, *Acta Crystallogr., Sect. A: Found. Crystallogr.*, 1995, 51, 909; V. A. Blatov and A. P. Shevchenko, *Acta Crystallogr., Sect. A: Found. Crystallogr.*, 2003, 59, 34.

54 Y. Tanabe and S. Sugano, *J. Phys. Soc. Jpn.*, 1954, 9, 753.

55 U.-C. Chung, J. L. Mesa, J. L. Pizarro, J. Rodríguez Fernández, J. Sánchez Marcos, J. S. Garitaonandia, M. I. Arriortua and T. Rojo, *Inorg. Chem.*, 2006, 45(22), 8965.

56 V. V. Guliants, J. B. Benziger and S. Sundaresan, *J. Catal.*, 1995, 156, 298.

57 X.-Z. Liao, Y.-S. He, Z.-F. Ma, X.-M. Zhang and L. Wang, *J. Power Sources*, 2007, 174, 720.

58 J. F. Moulder, W. F. Stickle, P. E. Sobol and K. D. Bomben, *Handbook of X-ray Photoelectron Spectroscopy (XPS)*, ed. J. Chastain, Physical Electronics Division, Perkin-Elmer Corporation, 1992–1995.

59 T. Yamashita and P. Hayes, *Appl. Surf. Sci.*, 2008, 254, 2441.

60 X. Wang, Y. Yan, J. Wu, Z. Dong, L. Li and J. Li, *Z. Anorg. Allg. Chem.*, 2013, 639(12–13), 2343.

61 L. F. Liotta, G. Di Carlo, G. Pantaleo, A. M. Venezia and G. Deganello, *Appl. Catal., B*, 2006, 66, 217.

62 I. de Pedro, J. M. Rojo, J. Rodríguez Fernández, M. T. Fernández-Díaz and T. Rojo, *Phys. Rev. B: Condens. Matter Mater. Phys.*, 2010, 81, 134431.

63 I. de Pedro, J. M. Rojo, J. M. Pizarro, J. Rodríguez Fernández, J. Sánchez-Marcos, M. T. Fernández-Díaz, M. I. Arriortua and T. Rojo, *J. Mater. Chem.*, 2007, 17, 3915; I. de Pedro, J. M. Rojo, J. L. Pizarro, J. Rodríguez Fernández, J. Sánchez-Marcos, M. I. Arriortua and T. Rojo, *J. Phys.: Condens. Matter*, 2006, 18, 3767; J. M. Rojo, J. L. Mesa, L. Lezama, J. L. Pizarro, M. I. Arriortua, J. Rodríguez Fernández, G. E. Barberis and T. Rojo, *Phys. Rev. B: Condens. Matter Mater. Phys.*, 2002, 66, 094406.

64 E. S. Larrea, J. L. Mesa, J. L. Pizarro, R. Fernández de Luis, J. Rodríguez Fernández, T. Rojo and M. I. Arriortua, *Dalton Trans.*, 2012, 41, 14170.